A: Kinetics, Dynamics, Photochemistry, and Excited States

Fingerprinting the Excited State Dynamics in Methyl Ester and Methyl Ether Anions of Deprotonated *para*-Coumaric Acid

James N Bull, Cate S. Anstöter, and Jan R. R. Verlet

J. Phys. Chem. A, **Just Accepted Manuscript** • DOI: 10.1021/acs.jpca.9b11993 • Publication Date (Web): 27 Feb 2020

Fingerprinting the Excited State Dynamics in Methyl Ester and Methyl Ether Anions of Deprotonated *para*-Coumaric Acid

James N. Bull,*,† Cate S. Anstöter,‡ and Jan R. R. Verlet‡

†*School of Chemistry, Norwich Research Park, University of East Anglia, Norwich NR4 7TJ, United Kingdom*
‡*Department of Chemistry, Durham University, Durham, DH1 3LE, United Kingdom*

E-mail: james.bull@uea.ac.uk

Abstract

Chromophores based on the *para*-hydroxycinnamate moiety are widespread in the natural world, including as the photoswitching unit in photoactive yellow protein and as a sunscreen in the leaves of plants. Here, photodetachment action spectroscopy combined with frequency- and angle-resolved photoelectron imaging is used to fingerprint the excited state dynamics over the first three bright action-absorption bands in the methyl ester anions (pCEs$^-$) of deprotonated *para*-coumaric acid at a temperature of ≈300 K. The excited states associated with the action-absorption bands are classified as resonances because they are situated in the detachment continuum and are open to autodetachment. The frequency-resolved photoelectron spectrum for pCEs$^-$ indicates that all photon energies over the $S_1\,(\pi\pi^*)$ band lead to similar vibrational autodetachment dynamics. The $S_2\,(n\pi^*)$ band is Herzberg-Teller active and has comparable brightness to the higher lying $2^1\,(\pi\pi^*)$ band. The frequency-resolved photoelectron spectrum over the $S_2\,(n\pi^*)$ band indicates more efficient internal conversion to the $S_1\,(\pi\pi^*)$ state for photon energies resonant with the Franck-Condon modes (≈80 %) compared with the Herzberg-Teller modes (≈60 %). The third action-absorption band, which corresponds to excitation of the $2^1\,(\pi\pi^*)$ state, shows complex and photon-energy-dependent dynamics, with 20–40 % of photoexcited population internally converting to the $S_1\,(\pi\pi^*)$ state. There is also evidence for a mode-specific competition between prompt autodetachment and internal conversion on the red edge of the $2^1\,(\pi\pi^*)$ band. There is no evidence for recovery of the ground electronic state and statistical electron ejection (thermionic emission) following photoexcitation over any of the three action-absorption bands. Photoelectron spectra for the deprotonated methyl ether derivative (pCEt$^-$) at photon energies over the $S_1\,(\pi\pi^*)$ and $S_2\,(n\pi^*)$ bands indicate diametrically opposed dynamics compared with pCEs$^-$, namely intense thermionic emission due to efficient recovery of the ground electronic state.

Introduction

Photoactive yellow protein (PYP) is a blue light sensor found in the *Halorhodospira halophila* bacterium.[1,2] In the PYP photocycle, absorption of blue light induces an ultrafast $E \rightarrow Z$ photoisomerization of the chromophore,[3–7] followed by a cascade of conformational changes of the host protein that ultimately cause the bacterium to move away from the light source.[8] The chromophore in PYP is a deprotonated phenolic-thioester molecule, which is structurally similar to the deprotonated methyl ester of *para*-(*E*)-coumaric acid (pCEs$^-$) shown in Figure 1. Although the importance of the sulphur atom and thioester linkage compared with a conventional ester linkage is not entirely clear, the pCEs$^-$ species is commonly assumed as a PYP model chromophore because it is easy to synthesize and does not decompose on standing. The fascinating photophysics of PYP and other photoactive proteins such as green fluorescent protein have contributed to development of the field of optogenetics,[9,10] which considers the application of genetically encoded photoswitch molecules to regulate biochemical processes.

Chromophores based on the *para*-coumaric acid moiety – so called *para*-hydroxycinnamate chromophores – are widespread in the Plantae kingdom,[11] where they function as photoprotecting sunscreens in the epidermal cell layers of plants. In this context, they have high absorption cross-sections for UV radiation and efficiently convert the absorbed energy into nuclear motion via an ultrafast internal conversion pathway along an $E \rightarrow Z$ isomerization coordinate. The efficacy of this mechanism has prompted the pharmaceutical and skincare industry to incorporate cinnamate molecules as UV-B filters in cosmetic sunscreens.[12]

A desire to understand the inherent photochemistry and excited state dynamics of *para*-hydroxycinnamate chromophores has led to a wide range of investigations. The majority of these studies were performed in solution, finding that the inherent $E \rightarrow Z$ photoisomerization efficiency and timescale is modified by deprotonation state and site, solvent interactions, functional group substitution and torsion-locking the single bond adjacent to the phenyl ring.[13–19] Theoretical investigations suggest there are barriers on the S_1 ($\pi\pi^*$) potential energy surface that dictate the molecule's photochemistry, and also suggest that functional group substitution and the presence of a condensed phase environment (solution or protein) can significantly alter the relative energetics/accessibility of conical intersection seams leading to $E \rightarrow Z$ isomerization.[20–27] In principle, the inherent photophysics can be disentangled from the influence of an environment by comparing photo-induced dynamics in the gas phase with those in condensed phases.

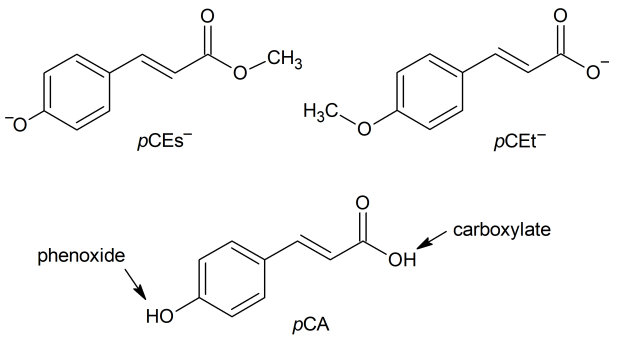

Figure 1: *E*-isomers of pCEs$^-$ and pCEt$^-$. *para*-coumaric acid, pCA, has two deprotonation sites, leading to phenoxide and carboxylate deprotomers.

In a pioneering gas-phase study, Zewail and coworkers[28] used femtosecond time-resolved photoelectron spectroscopy to study the dynamics on the $S_1(\pi\pi^*)$ state of a ketone derivative of pCEs$^-$, proposing that most of the photoexcited population survived for ≈52 ps before internally converting to the ground electronic state. Because this lifetime is long compared with the expected timescale for intramolecular vibrational energy redistribution,[29] the study concluded that internal conversion is a barrier controlled process. This conclusion was also reached by an earlier theoretical study using excited state molecular dynamics simulations.[20] In a recent contribution considering pCEs$^-$ (Figure 1), photodetachment action spectroscopy, single-color photoelectron spectroscopy and femtosecond time-resolved photoelectron imaging was used to demonstrate that some fraction of anions in the $S_1(\pi\pi^*)$ state internally converted to a dipole-bound state on a sub-picosecond timescale and the remainder of photoexcited anions relaxed to a twisted intermediate, which survived for ≈45 ps before autodetaching.[30] There was no evidence for recovery of the ground electronic state.

There have been several other gas-phase action spectroscopy studies utilizing nanosecond-duration pulsed light sources to elucidate on the absorption profiles and dynamics of electrosprayed hydroxycinnamate anions. These include photo-induced dissociation spectroscopy using an ultra-high vacuum ion storage ring,[31–33] infrared multiphoton dissociation (IRMPD) spectroscopy,[34] photoelectron spectroscopy,[35–38] and tandem ion mobility mass spectrometry.[39] For the simplest *para*-hydroxycinnamate molecule, *para*-coumaric acid (pCA, Figure 1), IRMPD and ion mobility studies have demonstrated that electrospray ionization produces both phenolate and carboxylate deprotomers,[34,39] and that the deprotomers have distinct photochemical responses. In particular, both deprotomers have partially overlapping action-absorption spectra in the 3.26–3.54 eV (380–350 nm) photon energy range and there is an efficient, *enol-keto* phototautomerizm and ensuing intramolecular proton transfer that converts the carboxylate deprotomer into the phenoxide deprotomer.[39] Typically, the yield of each deprotomer using electrospray ionization is largely influenced by the solvent and pH,[34,40] but can be also influenced by electrospray geometry and needle voltage, desolvation conditions, and collisional treatment of ions while introducing them into vacuum.[41,42] Unfortunately, for pCA$^-$, unknown depro-

tomer yields using electrospray ionization, overlapping action spectra for the two deprotomers with near-UV wavelengths of light and a photo-induced interconversion pathway between the deprotomers mean that the earlier photoelectron spectra are ambiguous. Overall, there is a clear need for benchmark measurements on the spectroscopy and excited state dynamics of isolated hydroxycinnamate anions with different functional group substitution and for which the deprotonation site is not in doubt.

Here, we have used photodetachment action spectroscopy and frequency- and angle-resolved photoelectron imaging to fingerprint the excited state dynamics for the first few electronic states of *p*CEs$^-$ and *p*CEt$^-$ (Figure 1). These anions were chosen because they allow for unambiguous study of phenoxide and carboxylate deprotonation sites, and because a recent tandem ion mobility study demonstrated that electrospray ionization of a sample of the *E*-isomer of each retains its geometric configuration in the absence of collisional activation (heating) in the electrospray ion source.[39] Our results show diametrically opposed excited state dynamics for the two anions, and highlight that multiple electron detachment pathways can contribute (often simultaneously) to low kinetic features in photoelectron spectra. Assuming that *p*CEs$^-$ and the thioester chromophore in PYP have similar gas-phase excited state dynamics, the lack of ground state recovery for any photon energy across the first three action-absorption bands for *p*CEs$^-$ implies that the protein environment in PYP plays a key role in tuning the photophysics of the chromophore.

Experimental

The photoelectron spectroscopy apparatus and frequency- and angle-resolved photoelectron imaging methodology has been described in detail elsewhere.[43–46] Briefly, gas-phase *p*CEs$^-$ or *p*CEt$^-$ was produced through electrospray (-5 kV) of a $\approx$1 mmol L^{-1} methanolic solution of the target compound (99%, Sigma-Aldrich, shielded from light) with a trace of ammonia. Electrosprayed anions were transferred *via* a capillary into a radio frequency ring-electrode ion trap. The trapped anions were unloaded (10 Hz) into a colinear time-of-flight optics assembly that accelerated them along a 1.3 m flight region and into a continuous-mode penetrating field velocity-mapping assembly.[44] Light pulses of a selected photon energy from a Continuum Horizon OPO pumped by a Continuum Surelite II Nd:YAG laser ($<$1 mJ pulse^{-1}, 5 ns pulse duration, 10 Hz) were timed to interact with the mass-selected ion packet at the centre of the velocity map imaging stack. Ejected electrons were velocity mapped onto a dual (chevron) multichannel plate (MCP) detector and P43 phosphor screen detector, which was monitored with a charge-coupled device camera. Velocity-map images were accumulated with a 500 ns acquisition gate applied to one of the MCPs. The velocity-mapping resolution is $\frac{\Delta E}{E}$ $\approx$5% and the electron kinetic energy (eKE) scale was calibrated from the spectrum of I$^-$. Velocity-map images were reconstructed using an antialiasing and polar onion-peeling algorithm,[47] providing the photoelectron spectra and associated angular distributions in terms of β_2 values.[48] β_2 values may range from –1 to 2,[48] with these limits corresponding to electron ejection perpendicular and parallel to the laser polarization, respectively. Quoted β_2 values in this work have an uncertainty of approximately $\pm$15%, providing qualitative assessment if β_2 values are positive, negative or zero (isotropic). In several measurements at selected photon energies, delay of the acquisition gate applied to the MCP by 50 ns relative to the light pulse tested for photoelectron signal associated with thermionic emission.[30,49]

Computational Details

Franck-Condon-Herzberg-Teller (FCHT) simulation of the absorption profiles for the first three bright electronic bands of *p*CEs$^-$ were performed using the Gaussian 16.B01 software package and FCHT algorithm implemented therein (includes Duschinsky rotation[50]).[51,52] The FCHT simulations assumed a temperature of 300 K in accord with the expected experimental trapping temperature. Geometry optimizations and vibrational frequency calculations as input for the FCHT simulations were performed at the ωB97X-D/aug-cc-pVDZ level of theory.[53,54] Vertical excitation energies (VEEs) were computed at the STEOM-DLPNO-CCSD/aug-cc-pVDZ level of theory using ORCA 4.2.0.[55,56]

Results and Discussion

Photodetachment action spectroscopy

*p*CEs$^-$

The photodetachment action spectrum for *p*CEs$^-$ is shown in Figure 2a. The spectrum has three clear bands, which are assigned to electronic transitions to the $S_1(\pi\pi^*)$, $S_2(n\pi^*)$ and $2^1(\pi\pi^*)$ states. The third bright state is labelled as $2^1(\pi\pi^*)$ rather than $S_3(\pi\pi^*)$ following the convention in the earlier photoelectron spectroscopy studies. Photon energies of maximum response over the three bands are $S_1(\pi\pi^*)$=2.88$\pm$0.02 eV, $S_2(n\pi^*)$=3.30$\pm$0.02 eV and $2^1(\pi\pi^*)$ $\approx$4.1 eV, with the latter given approximately due to overlap of the $2^1(\pi\pi^*)$ and $3^1(\pi\pi^*)$ bands. The maximum signal level over the $S_2(n\pi^*)$ and $2^1(\pi\pi^*)$ bands is $\approx$10% of that over the $S_1(\pi\pi^*)$ band.

The photodetachment action spectrum over the $S_1(\pi\pi^*)$ band (2.67–3.10 eV) was recently published in Ref. 30 with assignment of the vibrational structure having $\approx$90 cm^{-1} spacing to the principal Franck-Condon in-plane stretching vibration, ν_3=88 cm^{-1}

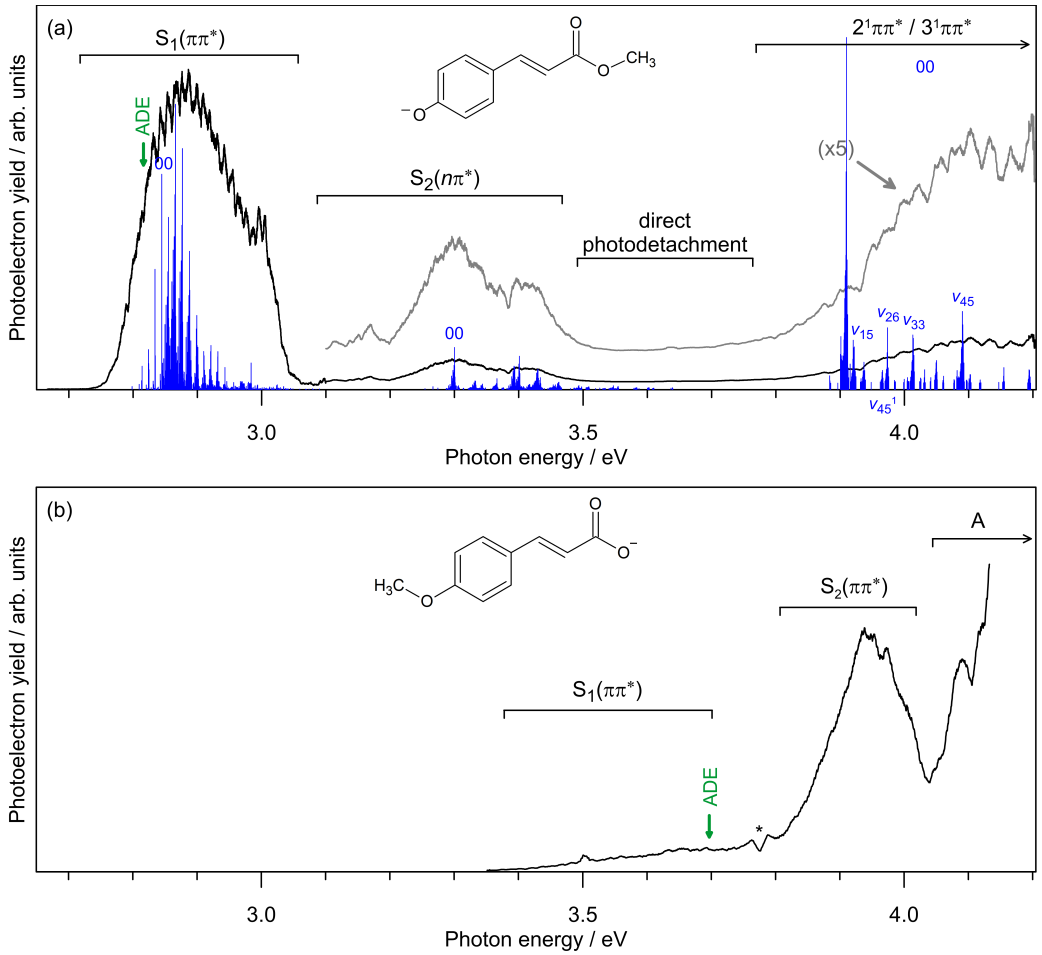

Figure 2: Photodetachment action spectra: (a) pCEs$^-$, with the gray trace as a five-fold magnification of the black trace; (b) pCEt$^-$. FCHT simulations (blue, arbitrary scaled) are included for pCEs$^-$ and have been translated for best agreement with experiment. The feature denoted with * in (b) is probably an artefact. Note, pCEt$^-$ signal extends below the ADE by ≈0.16 eV because ions at a temperature of 300 K have ≈0.15 eV vibrational energy (calculated from a harmonic partition function). In (a), FCHT simulations at the ωB97X-D/aug-cc-pVDZ level of theory were shifted by -0.41 eV [$S_1(\pi\pi*)$], -0.50 eV [$S_2(n\pi*)$] and -0.39 eV ($2^1\pi\pi^*$) to achieve best agreement with experiment. Note, it is difficult to align the FCHT simulation for the $2^1\pi\pi^*$ state with experiment due to the absence of clear vibrational structure.

(ωB97X-D/aug-cc-pVDZ level of theory).[30] The rest of the present photodetachment action spectrum, i.e. over the higher photon energy bands, agrees with a photoneutralization spectrum for pCEs$^-$ recorded using an ultrahigh vacuum ion storage ring,[33] except offers increased spectral resolution. For pCEs$^-$, we expect that the photodetachment action spectrum should parallel the gas-phase absorption spectrum because there was no evidence for statistical electron ejection (thermionic emission) at any photon energy across the action spectrum range and thus our measurement should capture all ejected electrons, the origin of the $S_1(\pi\pi^*)$ band is above the adiabatic detachment energy, ADE = 2.83±0.05 eV,[30] the electronic transitions are bright (large absorption cross-section) compared with the direct photodetachment baseline, and fluorescence should be negligible due to the picosecond lifetime of the $S_1(\pi\pi^*)$ state.[30]

Calculated vertical excitation energies (VEEs) for pCEs$^-$ at the STEOM-DLPNO-CCSD/aug-cc-pVDZ (ωB97X-D/aug-cc-pVDZ geometry) level of theory and oscillator strengths (f) are given in Table 1, revealing reasonable agreement with experiment. The largest deviation between theory and experiment is for the $S_2(n\pi^*)$ state, with the calculated VEE being ≈0.2 eV larger than experiment. For comparison, EOM-CC3/aug-cc-pVDZ (RI-MP2/6-31+G* geometry) VEE values from Ref. 39 are in excellent agreement with experiment for the $S_1(\pi\pi^*)$ and $S_2(n\pi^*)$ states, however, the VEE for the $2^1(\pi\pi^*)$ state is ≈0.3 eV lower in energy than experiment. We propose that the poorer agreement between the calculated and experimental VEE for the $2^1(\pi\pi^*)$ state at the higher level of theory (EOM-CC3/aug-cc-pVDZ) is due to the initial geometry. For example, repeating the STEOM-DLPNO-CCSD/aug-cc-pVDZ calculation at the RI-MP2/6-31+G* geometry, i.e. the geometry used in the EOM-CC3 calculation, leads to a decrease of the calculated VEE

for the $2^1(\pi\pi^*)$ state by ≈0.2 eV, yet there is little change in VEE for the other two states. It is also worth noting that the STEOM-DLPNO-CCSD/aug-cc-pVDZ (ωB97X-D/aug-cc-pVDZ geometry) calculations gave VEE=4.28 eV (f = 0.02) for the $3^1(\pi\pi^*) \leftarrow S_0$ transition, suggesting overlap with the blue-edge of the $2^1(\pi\pi^*)$ band.

The photodetachment action spectrum for pCEs$^-$ shows that the maximum signal level over the $S_2(n\pi^*)$ band reaches ≈10% of that for the $S_1(\pi\pi^*)$ band, which is substantially more intense than predicted from the calculated oscillator strengths. It is unlikely that the direct photodetachment cross-section ($D_0 \leftarrow S_0$) varies significantly over the two transitions, and therefore does not account for this disagreement between experiment and theory. A feasible explanation is provided by FCHT simulation of the $S_2(n\pi^*) \leftarrow S_0$ transition at a temperature of 300 K, which predicts that the intensity of the $S_2(n\pi^*)$ band is significantly increased through Herzberg-Teller coupling.[57–59] Specifically, the FCHT simulation predicts that ≈80% of the band intensity originates from Herzberg-Teller active combination modes and provides a simulated absorption profile that satisfactorily accounts for the shape of the action spectrum (the simulation has been translated in photon energy for best agreement with experiment), with the lower energy part of the $S_2(n\pi^*)$ band principally defined by Franck-Condon modes and the higher energy part by Herzberg-Teller modes. Further details of the Franck-Condon vs Herzberg-Teller modes are given in the Supporting Information. Finally, the small feature in the $h\nu$ = 3.1–3.2 eV window might be due to hot band signal not accounted for in the FCHT simulation (e.g. some fraction of the ions at higher temperature) or possibly a contribution from the alternative rotamer (see calculations and discussion later).

A FCHT simulation of the $2^1(\pi\pi^*) \leftarrow S_0$ transition for pCEs$^-$ is shown in Figure 2a, which has been translated in photon energy for approximate agreement with experiment. The simulation predicts that the transition is origin dominated with some intensity associated with several in-plane modes: ν_{15} = 516 cm^{-1} (phenyl stretch), ν_{26} = 838 cm^{-1} (phenyl breathing), ν_{33} = 1128 cm^{-1} (phenyl hydrogen wag), and ν_{45} = 1459 cm^{-1} (phenyl stretching). Although the simulation predicted hot band signal at a temperature of 300 K, the experimental spectrum is still considerably broadened on the red edge with no clear origin transition. Two possible reasons for the difference between experiment and theory are: (1) a short inherent lifetime of the $2^1(\pi\pi^*)$ state due to the shape resonance character of the state, and (2) transition smearing associated with fluxionality/rotamers of the ground electronic state anions in the gas phase at a temperature of 300 K (more so for the $2^1(\pi\pi^*)$ state than the other two states).

Table 1: Experimental and calculated vertical excitation energies (VEEs) in eV and oscillator strengths (f) for pCEs$^-$.

State	Experiment	Theory[a]	f	Ref. 39
$S_1(\pi\pi^*)$	2.88±0.02	2.80	0.9	2.88
$S_2(n\pi^*)$	3.30±0.02	3.50	3×10^{-3}	3.22
$2^1(\pi\pi^*)$	≈4.1[b]	4.06	0.1	3.78

[a]Calculated values are at the STEOM-DLPNO-CCSD/aug-cc-pVDZ (ωB97X-D/aug-cc-pVDZ geometry) level of theory. [b]Estimated value – see text for comparison with other action spectroscopy measurements.

The first spectral broadening factor, an inherently short lifetime of the $2^1(\pi\pi^*)$ state, presumably has some contribution since the state is classified as a shape resonance,[60] i.e. a one-electron detaching transition is required to achieve the neutral state. Time-resolved measurements on the dynamics of resonances for other gas-phase chromophores by the current authors have found that shape resonances situated well into the detachment continuum (as is the case here) usually have sub-60 fs lifetimes. As a specific example, cryogenic photodetachment action spectroscopy measurements on the first shape resonance in the *para*-benzoquinone radical anion show a broad, featureless electronic transition due to lifetime broadening.[45,61] Femtosecond time-resolved measurements determined that the shape resonance in that instance had a lifetime of ≈20 fs.[62] In contrast, Feshbach resonances near the detachment threshold in cold *para*-benzoquinone radical anions produced clear vibrational structure and therefore have much longer lifetimes.[61] Returning to the $2^1(\pi\pi^*)$ state of pCEs$^-$, excited state lifetimes in the range 10–40 fs correspond to spectral widths of 0.4–0.1 eV, which could satisfactorily explain the lack of a sharp origin transition and breadth of the action spectrum band.

The second spectral broadening factor, smearing of the $2^1(\pi\pi^*) \leftarrow S_0$ transition energy due to fluxionality/rotamers, is consistent with the VEE calculations above that demonstrated a sensitivity of this transition energy to the initial geometry (much more so than for the other two states). Furthermore, a recent study considering deprotomers of pCA$^-$ used RRKM calculations to propose that the phenoxide deprotomer in the gas phase (and presumably also pCEs$^-$) are rigid towards internal rotation at a temperature of 300 K and, consequently, exist in two rotameric forms. Calculations on the higher-energy rotamer at the STEOM-DLPNO-CCSD/aug-cc-pVDZ level of theory gave VEEs of $S_1(\pi\pi^*)$=2.81 eV, $S_2(n\pi^*)$=3.17 eV and $2^1(\pi\pi^*)$=3.87 eV. The VEE for the $S_1(\pi\pi^*) \leftarrow S_0$ transition is within 0.01 eV of that for the most stable deprotomer, and the VEE for the $S_2(n\pi^*)$ state (perhaps fortuitously) is consistent with a minor unassigned feature situated just below $h\nu$ = 3.2 eV in the photodetachment spectrum (Figure 2a). The calculated VEE for the $2^1(\pi\pi^*) \leftarrow S_0$ transition of the rotamer is ≈0.2 eV lower in energy than that for the most stable rotamer, again consistent with spectral smearing of the origin transition. At this stage, it is unclear which spectral

Table 2: Experimental and calculated vertical excitation energies (VEEs) in eV and oscillator strengths (f) for pCEt$^-$.

State	Experiment	Theory[a]	f	Ref. 39
$S_1(\pi\pi^*)$	$\approx$3.6[b]	4.28	0.3	3.51
$S_2(\pi\pi^*)$	3.93$\pm$0.02	4.48	0.03	4.06

[a]Calculated values are at the STEOM-DLPNO-CCSD/aug-cc-pVDZ (ωB97X-D/aug-cc-pVDZ geometry) level of theory. [b]Estimated value – see text for comparison with other action spectroscopy measurements.

broadening mechanism is dominant.

pCEt$^-$

The photodetachment action spectrum for pCEt$^-$ (Figure 2b) has two bands and the shoulder of a third, which is denoted by 'A'. The first two bands are assigned to the $S_1(\pi\pi^*) \leftarrow S_0$ and $S_2(\pi\pi^*) \leftarrow S_0$ transitions. This photodetachment action spectrum has two contrasting properties compared with pCEs$^-$. First, a significant portion of the $S_1(\pi\pi^*)$ band is situated below the ADE (determined at 3.7$\pm$0.2 eV later). Second, delay of the acquisition gate on the detector by 50 ns relative to the light pulse showed that thermionic emission is the dominant electron detachment pathway. These two properties imply that the photodetachment action spectrum for pCEt$^-$ will vary from the inherent absorption spectrum. Specifically, our photodetachment acquisition collected electrons ejected over a 500 ns window after the light pulse – this acquisition gate is required for velocity-map imaging. Assuming thermionic emission operates on a tens to hundreds microsecond timescale (varies with photon energy and might be in competition with statistical dissociation), the photodetachment measurement collects only a few percent of the total electron detachment yield.

Calculated VEEs for pCEt$^-$ at the STEOM-DLPNO-CCSD/aug-cc-pVDZ (ωB97X-D/aug-cc-pVDZ geometry) are summarized in Table 2, revealing that this level of theory overestimates by >0.6 eV compared with experiment. For comparison, the VEEs at the EOM-CC3/aug-cc-pVDZ level of theory from Ref. 39 are in much better agreement with experiment, with the reference study concluding that at least the aug-cc-pVDZ basis set as well as corrections for triples excitations in the EOM methodology are required to align calculated VEEs with action spectra for the carboxylate deprotomer of pCA$^-$.[39] While the VEEs for pCEt$^-$ at the EOM-CC3/aug-cc-pVDZ level of theory are consistent with the present photodetachment action spectrum, the oscillator strengths deviate from experiment because much of the $S_1(\pi\pi^*)$ band is situated below the detachment threshold. Feature 'A' in the photodepletion action spectrum for pCEt$^-$ (Figure 2b) is presumably due to excitation of a higher lying electronic state.

The pCEt$^-$ photodetachment action spectrum has an appearance threshold at $\approx$3.35 eV and a photon energy of maximum response over the $S_2(\pi\pi^*)$ band at $\approx$4.0 eV. Both of these properties are similar to those found for pCEt$^-$ in a recent photodepletion action spectrum recorded using a tandem ion mobility spectrometer.[39] Unfortunately, it is difficult to provide a more detailed comparison due to the high pressure environment in the tandem ion mobility spectrometer and consequential quenching of statistical processes such as thermionic emission.[63] In an alternative comparison, the tandem ion mobility spectrometry study reported an action spectrum for the $S_1(\pi\pi^*) \leftarrow S_0$ transition of the carboxylate deprotomer of pCA$^-$ by monitoring phototautomerization and ensuing intramolecular rearrangement.[39] Theoretical modelling revealed that the initial phototautomerization involved an excited state mechanism that should occur faster than collisional energy quenching. Although phototautomerization does not occur for pCEt$^-$, the phototautomerization action spectrum for the carboxylate deprotomer of pCA$^-$ has maximum response at $\approx$3.5 eV, which is close to the calculated VEE for that deprotomer and also for pCEt$^-$ at 3.51 eV from Ref. 39. This is consistent with assignment of $S_1(\pi\pi^*)$ band for pCEt$^-$ in Figure 2b. FCHT simulation of the absorption spectrum for pCEt$^-$ was not attempted since the present action spectrum does not mirror the absorption spectrum.

Frequency- and angle-resolved photoelectron imaging

Frequency- and angle-resolved photoelectron imaging was used to provide spectral fingerprints for excited state dynamics in pCEs$^-$ and pCEt$^-$. The underlying strategy of the technique is to maximize information content by recording a series of photoelectron spectra with varying photon energy and analyzing trends in the electron kinetic energy (eKE) distributions and their angular properties.[45,46,64] When these data are considered along with the photodetachment action spectrum and photoelectron spectra in which the acquisition gate applied to the MCP detector is delayed relative to the light pulse,[49] certain spectral features and trends can provide indirect evidence or "fingerprints" for excited state dynamics. Potential dynamical fingerprints include internal conversion between resonances, vibrational autodetachment from excited states situated below the detachment threshold, and recovery of the ground electronic state followed by thermionic emission.

pCEs$^-$: $S_1(\pi\pi^*)$ band

The frequency-resolved spectrum for pCEs$^-$ is shown in Figure 3a and the photodetachment action spectrum is reproduced in Figure 3b for direct comparison. The 41 photoelectron spectra contributing to the frequency-resolved spectrum have been area normalized to accentuate the spectral features. Photoelectron angular distributions in terms of β_2 values are shown in Figure 3c.

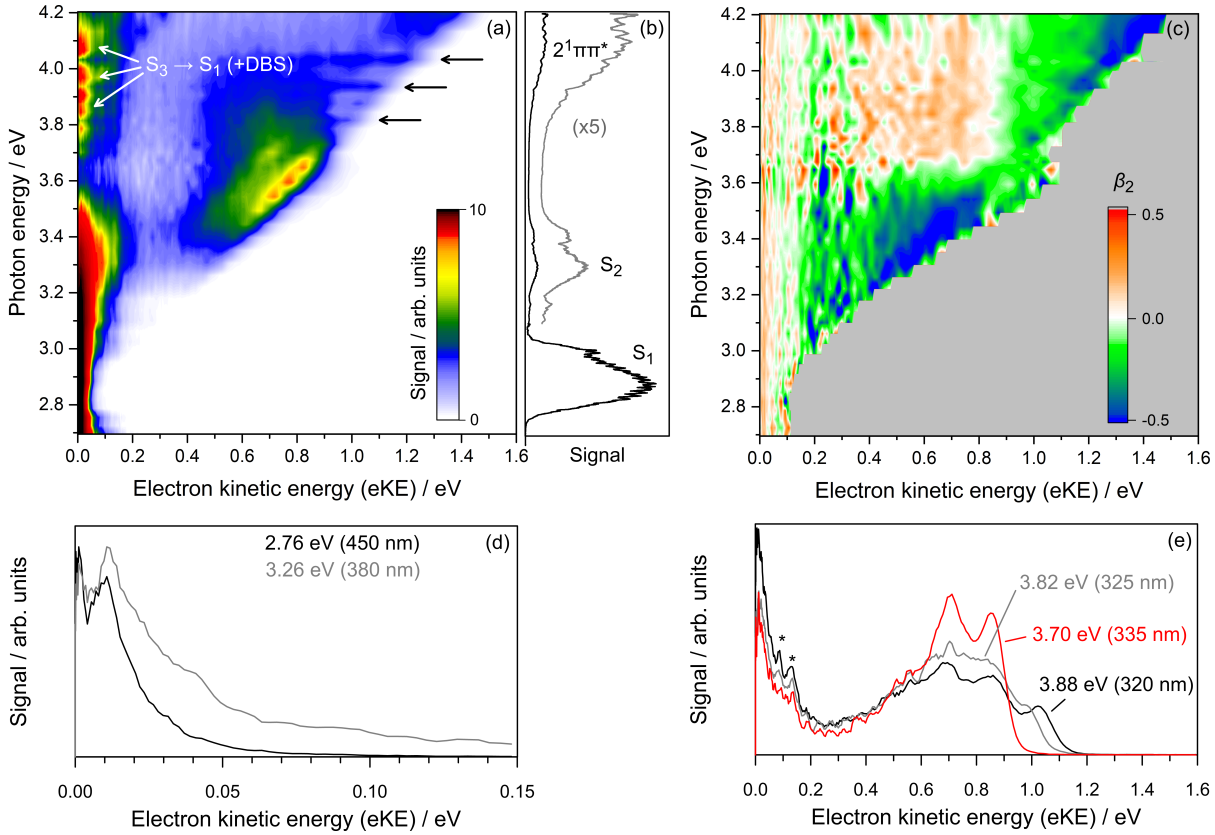

Figure 3: Frequency-resolved photoelectron spectroscopy of pCEs$^-$: (a) frequency-resolved photoelectron spectrum, (b) photodetachment action spectrum for visual comparison with (a), (c) photoelectron angular distributions in terms of β_2 values, (d) example photoelectron spectra at $h\nu$ = 2.76 and 3.26 eV associated with resonant excitation of the $S_1(\pi\pi^*)$ and $S_2(n\pi^*)$ bands, (e) example photoelectron spectra at $h\nu$ = 3.70, 3.82 and 3.88 eV associated with resonant excitation of the $2^1(\pi\pi^*)$ band. Note the different horizontal abscissa scales. See SI for all individual spectra contributing to (a). The * symbols in (e) are discussed in the text.

The frequency-resolved spectrum (Figure 3a) shows a low-eKE distribution over the $2.7 \leq h\nu \leq 3.1$ eV range, i.e. over the $S_1(\pi\pi^*)$ band, with double peak structure – see example photoelectron spectra in Figure 3d. The spectrum at $h\nu$ = 2.76 eV is essentially identical to the photoelectron spectra at all other photon energy over the $S_1(\pi\pi^*)$ band. A recent study on pCEs$^-$ combining single-color photoelectron spectroscopy and femtosecond time-resolved photoelectron spectroscopy assigned this double peak structure to the combination of nuclear relaxation to a twisted intermediate geometry on the $S_1(\pi\pi^*)$ state followed by autodetachment and vibrational autodetachment from a dipole-bound state.[30] Photoelectron angular distributions show that $\beta_2 \approx +0.1$ over the low-eKE feature, and delay of the acquisition gate applied to the MCP detector by 50 ns relative to the light pulse confirmed that all photoelectron signal occurred within 50 ns. Both of these results are consistent with no thermionic emission, which should yield low-eKE electrons with an isotropic photoelectron angular distribution ($\beta_2 \approx 0$) over a microsecond timescale. It follows that most of the $S_1(\pi\pi^*)$ population undergoes nuclear relaxation to form either a twisted intermediate or dipole-bound state, both of which autodetach.[30]

The photoelectron spectra associated with the blue edge of the $S_1(\pi\pi^*)$ band show a small amount of prompt detachment, defined as a combination of direct photodetachment and prompt autodetachment, e.g. <10% in the $h\nu$ = 3.00 eV spectrum, with the signal in the 0.05–0.15 eV window having $\beta_2 \approx -0.4$.

pCEs$^-$: $S_2(n\pi^*)$ band

The frequency-resolved spectrum in Figure 3a shows that photon energies resonant with the low photon energy ($h\nu$ = 3.15–3.35 eV) part the $S_2(n\pi^*)$ band, i.e. associated with predominately Franck-Condon modes as discussed in the Supporting Information, yields mostly low-eKE signal with $\beta_2 \approx +0.1$. Because this signal resembles that when exciting the $S_1(\pi\pi^*)$ state, we assign the dynamics as internal conversion and autodetachment from the $S_1(\pi\pi^*)$ twisted intermediate and dipole-bound state. Such dynamics are consistent with the Feshbach resonance character of the $S_2(n\pi^*)$, which requires electron reconfiguration to achieve the neutral electronic structure in during autodetachment and allows a time window for internal conversion to occur.

For photon energies resonant with the remainder of

the $S_2(n\pi^*)$ band ($h\nu$ = 3.35–3.50 eV), Herzberg-Teller active modes dominate the photodetachment action spectrum (see Supporting Information) and the photoelectron spectra show two significant changes. First, the amount of low-eKE signal decreases, broadens and loses the double peaked structure that was attributed to some combination of vibrational autodetachment from the $S_1(\pi\pi^*)$ state and a dipole-bound state. Second, β_2 values over the low-eKE feature are closer to zero ($\beta_2 \approx$+0.05), but β_2 values over the remainder of the frequency-resolved spectrum are negative, reaching $\beta_2 \approx$-0.5 on the high-eKE tail. Delay of the acquisition gate applied to the MCP detector by 50 ns confirmed that there is no thermionic emission.

In summary, the frequency-resolved spectrum associated with the $S_2(n\pi^*)$ band indicates that resonant access of Franck-Condon and Herzberg-Teller excited state modes lead to distinct non-adiabatic dynamics. Undoubtedly, future investigations employing cryogenic methods will allow for measurement of vibrational structure over the $S_2(n\pi^*)$ band. Time-resolved photoelectron spectroscopy could further elucidate on the dynamics associated with each section of the $S_2(n\pi^*)$ band.[30]

*p*CEs$^-$: Direct photodetachment region

We term the region between the $S_2(n\pi^*)$ and $2^1(\pi\pi^*)$ bands ($h\nu \approx$3.5–3.7 eV in Figure 2a and Figure 3a) in the *p*CEs$^-$ photodetachment action spectrum the 'direct photodetachment region'. In this region, the photoelectron spectra are dominated by a high-eKE distribution with a peak eKE that increases commensurately with photon energy and is consistent with predominately direct photodetachment. Photoelectron angular distributions are aligned perpendicular to the laser polarization, with $\beta_2 \approx$-0.5 over the central part of the direct photodetachment region.

It is worth noting that there is a small yield of low-eKE electrons with a doubled peaked distribution (<5% of the photoelectron signal) with slightly positive β_2 values produced over the direct photodetachment region. This is presumably from smearing of the red-edge of the $2^1(\pi\pi^*) \leftarrow S_0$ transition, as discussed above.

Many of the photon energies used in earlier photoelectron studies[35–38] to imply excited state dynamics in *p*CEs$^-$ and derivatives used photon energies over this direct photodetachment region (e.g. 3.54, 3.87 and 3.94 eV in Ref. 36). These photoelectron spectra were interpreted in terms of dynamics associated with the $2^1(\pi\pi^*)$ state and internal conversion to give thermionic emission. Both the present and our earlier study[30] show that there is no internal conversion to the ground electronic state and no thermionic emission.

*p*CEs$^-$: $2^1(\pi\pi^*)$ band

The frequency-resolved spectrum for *p*CEs$^-$ over the $2^1(\pi\pi^*)$ band ($h\nu \approx$3.7–4.2 eV in Figure 2a and 3a) reveals complex fingerprints of excited state dynamics. There was no evidence for thermionic emission using the detector gating strategy. The photoelectron spectra can be broadly divided into three regions. First, from the onset of the $2^1(\pi\pi^*)$ band at $h\nu \approx$3.7 eV to $h\nu \approx$4.1 eV, the frequency-resolved spectrum has a static eKE distribution centred at eKE≈0.7 eV with $\beta_2 \approx$+0.2 – see the eKE = 0.3–0.9 eV region in Figure 3c. Second, there is a substantial fraction of low-eKE signal that is consistent with some fraction of excited state population undergoing internal conversion and autodetachment from the twisted intermediate on the $S_1(\pi\pi^*)$ state and a dipole-bound state. Third, the high-eKE distributions show vibrational structure at certain photon energies. There is also a modulation in intensity between low-eKE signal and high-eKE signal with photon energy, which is indicative of vibrational mode-specific dynamics (see arrows in Figure 3a). The modulation between low-eKE and high-eKE photoelectron signal is illustrated by the $h\nu$ = 3.82 and 3.88 eV photoelectron spectra in Figure 3e. These three properties/trends are now discussed in turn.

The static eKE distribution centred at eKE≈0.7 eV occurs over the $h\nu \approx$3.6–4.1 eV range and could originate from three processes: (i) internal conversion to the $S_2(n\pi^*)$ state followed by autodetachment, (ii) nuclear relaxation on the $2^1(\pi\pi^*)$ followed by autodetachment, and (iii) prompt autodetachment that occurs more rapidly than any vibrational energy redistribution so that vibrational excitation of the anion is retained during the detaching transition. Explanation (i) is consistent with the energy of the $S_2(n\pi^*)$ state, which is situated ≈0.5–0.6 eV above the ADE. Explanation (ii) is consistent with calculations on the optimized geometry of the $2^1(\pi\pi^*)$, which predict that the state is situated ≈0.7 eV above the detachment threshold. Explanation (iii) might be consistent with the shape resonance character of the state, however, rotamer/geometry smearing complicate any firm assignment. The significant change in β_2 value across the static eKE distribution no doubt contains important dynamical information, however, there is no simple way to model angular distributions associated with autodetachment from resonances. Whatever the assignment, it is interesting to note that similar trends in frequency-resolved spectra and associated β_2 values have been previously observed for the *para*-HBDI$^-$ (chromophore in green fluorescent protein) when exciting over the red edge of the $2^1(\pi\pi^*)$ band,[65] and also for several other *para*-substituted phenoxide anions.[66] Time-resolved spectroscopy on the $2^1(\pi\pi^*)$ state of *para*-HBDI$^-$ showed that the excited state dynamics leading to the eKE distribution occurred on a sub-60 fs timescale.[65] The initial interpretation of the *para*-HBDI$^-$ results followed the first explanation (internal conversion followed by autodetachment), with the assignment in part attributed to a sudden change in β_2 values with photon energy. Subsequently, Bochenkova et al.[67] suggested through calculations that explanation (iii) was most likely, although their calcula-

tions did not account for the sudden change in β_2 values. Very recently, Glover et al.[68] used high-level theory to identify a conical intersection and internal conversion route lending support to the original assignment.

The low-eKE feature in the frequency-resolved spectrum over the $h\nu$ = 3.7–4.0 eV range, which has $\beta_2 \approx +0.1$, is consistent with internal conversion and autodetachment from the twisted intermediate on the $S_1(\pi\pi^*)$ state and a dipole-bound state. Integrating the low-eKE signal (eKE<0.2 eV) in the frequency-resolved spectrum indicates that it constitutes 20–40% of the photoelectron signal. It is unknown if the internal conversion mechanism leading to the low-eKE signal is a direct $2^1(\pi\pi^*) \rightarrow S_1(\pi\pi^*)$ process or the $S_2(n\pi^*)$ state is involved as an intermediate, i.e. a $2^1(\pi\pi^*) \rightarrow S_2(n\pi^*) \rightarrow S_1(\pi\pi^*)$ internal conversion cascade. It is worth noting that the low-eKE photoelectron features for photon energies over the $2^1(\pi\pi^*)$ and $S_2(n\pi^*)$ bands show reproducible structure indicated by the * in Figure 3e (see individual spectra in the Supporting Information), however, this structure is not evident in photoelectron spectra for photon energies across the $S_1(\pi\pi^*)$, indicating differing vibrational autodetachment dynamics following direct excitation of the $S_1(\pi\pi^*)$ state or access through internal conversion. In earlier photoelectron spectroscopy studies on quinone cluster anions, we assigned structured, low-eKE features to autodetachment from a dipole-bound or correlation-bound state,[69,70] with the vibrational structure attributed to specific autodetaching vibrational modes.[71] In this mechanism, vibrational motion associated with modulation of the orbital containing the most weakly bound electron causes the electron to be "shaken off" with a kinetic energy proportional to the vibrational mode frequency. Ultimately, time-resolved photoelectron spectroscopy is the best avenue for gaining further insight into internal conversion and low-eKE vibrational autodetachment dynamics associated with the $2^1(\pi\pi^*)$ state, although such measurements should be performed at low temperatures to minimize spectral smearing associated with ion fluxionality.

The high-eKE vibrational structure in the photoelectron spectra consists of three obvious vibrations occurring at fixed eKE values (i.e. they do not move with photon energy) of 0.70, 0.86 and 1.02 eV (±0.03 eV uncertainty), corresponding to a spacing of ≈0.16 eV or ≈1300 cm^{-1}. The example photoelectron spectra in Figure 3e show two of these vibrations in the $h\nu$ = 3.70 eV spectrum and three in the and $h\nu$ = 3.88 eV spectrum. Furthermore, the high-eKE vibrational structure and the modulation in spectral intensity between the low-eKE and high-eKE signal with photon energy (spacing of ≈0.12 eV) appear connected – the high-eKE vibrational structure is evident for photon energies that give reduced low-eKE signal, while the high-eKE vibrational structure is washed out for photon energies that give increased low-eKE signal. There is no clear vibrational structure in the photodetachment action spectrum consistent with either the high-eKE vibrational structure or the modulation between low-eKE and high-eKE signal with photon energy. The lack of any new detaching transitions in a direct photodetachment simulation ($D_0 \leftarrow S_0$) implies that the direct photodetachment cross-section should not sharply change over the $2^1(\pi\pi^*) \leftarrow S_0$ transition.

Taking all of the data together and remembering that the photodetachment action spectrum showed a broadened red edge for the $2^1(\pi\pi^*) \leftarrow S_0$ transition, a possible explanation for the high-eKE vibrational structure and the modulation in spectral intensity between the low-eKE and high-eKE signal with photon energy is schematically illustrated in Figure 4. We propose that there is a mode-specific excited state competition between prompt autodetachment and internal conversion. In this mechanism, resonant excitation of vibrational levels of one or several specific modes – say including the ν_{45} = 1459 cm^{-1} (phenoxide stretch) – leads to increased prompt autodetachment signal compared with resonant excitation of other modes (e.g. the 0-0 transition or ν_{15}, ν_{26} and ν_{33} modes), which give more efficient internal conversion. We selected ν_{45} = 1459 cm^{-1} as a possible example mode because very fast autodetachment from this vibration to corresponding neutral vibrations could account for both the spacing in the high-eKE vibrational structure and the (approximate) photon energy spacing for eKE modulation in the frequency-resolved spectrum. It is worth noting that a similar modulation between low-eKE and high-eKE signal when photoexciting over a shape resonance was observed in photoelectron spectroscopy study on coen-

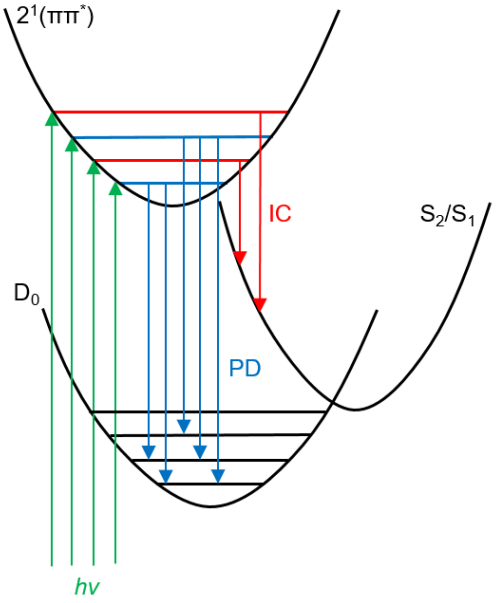

Figure 4: Proposed photo-induced electron ejection dynamics associated with the red edge of the $2^1(\pi\pi^*) \leftarrow S_0$ transition for pCEs$^-$. PD indicates a prompt autodetachment process for the ν = 1459 cm^{-1} mode (blue), and IC (red) indicates an internal conversion to the $S_1(\pi\pi^*)$ state possibly via the $S_2(n\pi^*)$ state.

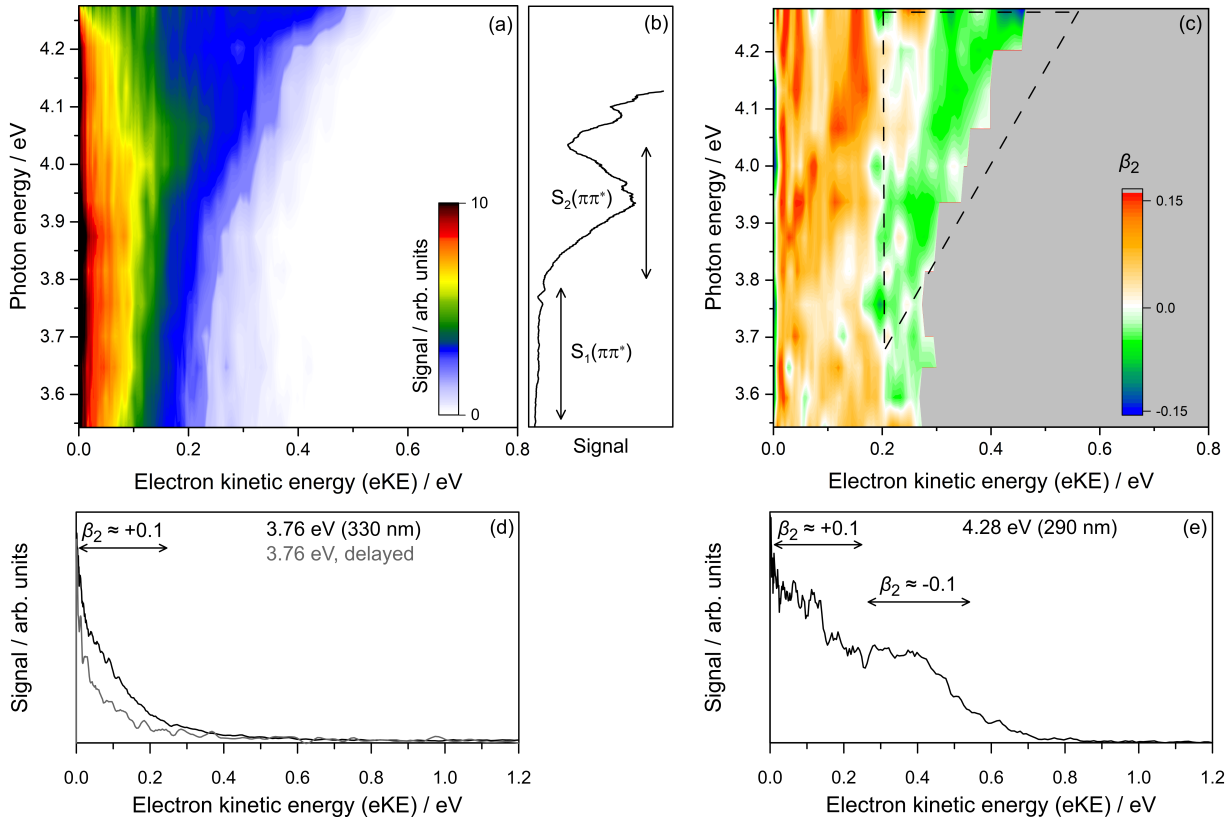

Figure 5: Frequency-resolved photoelectron spectroscopy of pCEt$^-$: (a) frequency-resolved photoelectron spectrum, (b) photodetachment action spectrum for visual comparison with (a), (c) corresponding photoelectron angular distributions in terms of β_2 values, (d) example photoelectron spectra at $h\nu = 3.76$ eV without (black) and with (gray) delay of the MCP acquisition gate by 50 ns, (e) example photoelectron spectrum at $h\nu = 4.25$ eV. Note the different horizontal abscissas. See SI for all individual spectra contributing to (a).

zyme Q_0 dimer radical anions,[69] and was similarly interpreted as a mode-specific excited state competition between prompt autodetachment and internal conversion. Finally, we note that the proposed interpretation in Figure 4 requires that the initial anion geometry is well defined, thus, if our hypothesis is correct, broadening of the red edge of the photodetachment action spectrum over the $2^1(\pi\pi^*) \leftarrow S_0$ transition is due to lifetime broadening of the origin transition.

For photon energies higher than $h\nu \approx 4.1$ eV, there is new signal at low-eKE that appears to increase in peak eKE commensurately with photon energy, and is assigned to a new direct photodetachment channel. EOM-IP-CCSD/aug-cc-pVDZ calculations gave the second vertical detachment energy (VDE) for pCEs$^-$ at 4.36 eV,[39] which consistent with this new feature ($D_1 \leftarrow S_0$). Photoelectron spectra were not recorded for photon energies higher than $\approx$4.2 eV due to background from photoelectrons associated with scattered light striking the velocity-mapping electrodes.

In summary, the $2^1(\pi\pi^*)$ state of pCEs$^-$ exhibits complex internal conversion and mode-specific autodetachment dynamics. These dynamics were not recognized in earlier photoelectron spectroscopy studies targeting this state. Undoubtedly, future investigations on cryocooled anions will provide increased spectral resolution and further insight into the excited state dynamics associated with the $2^1(\pi\pi^*)$ band.

pCEt$^-$

The frequency-resolved spectrum for pCEt$^-$ is shown in Figure 5a and the photodetachment action spectrum is reproduced in Figure 5b for direct comparison. The 13 photoelectron spectra contributing to the frequency-resolved spectrum have been area normalized to accentuate spectral features. Photoelectron angular distributions in terms of β_2 values are shown in Figure 5c.

The frequency-resolved spectrum shows there is a low-eKE feature (eKE <0.2 eV) for all studied photon energies, exemplified by the $h\nu = 3.76$ eV spectrum in Figure 5d. This low-eKE feature has three important properties: (i) it does not comply to a single exponential-like distribution (and has a different shape to that for pCEs$^-$), rather there is a weak shoulder at eKE$\approx$0.05 eV which is evident for photon energies above and below the ADE; (ii) $\beta_2 \approx +0.1$ over the low-eKE feature (see Figure 5c), which is inconsistent with purely thermionic emission; (iii) delay of the acquisition gate applied to the MCP detector by 50 ns relative to the light pulse produced photoelectron spectra like that shown in Figure 5d, gray, which has $\beta_2 \approx 0$ (isotropic electron ejec-

tion) and is consistent with some contribution from thermionic emission – similar thermionic emission signal was observed when using MCP gating at *all* photon energies in Figure 5a. These three properties of the low-eKE signal in the frequency-resolved spectrum for pCEt$^-$ suggest the low-eKE signal is due to a combination of vibrational autodetachment and thermionic emission, with the weak shoulder at eKE≈0.05 eV presumably due to the vibrational autodetachment process. It is also possible that there is some contribution from a dipole-bound state since the neutral core of pCEt has a calculated dipole moment of μ=4.8 D (anion geometry), which exceeds the ≈2.5 D threshold to support a dipole-bound state.[72] Whether dipole-bound states are involved during internal conversion to recover the ground electronic state is a topical question with relevance to a range of common photochemical moieties,[30] but cannot be reliably probed through single-color photoelectron spectroscopy.

The frequency-resolved spectrum for pCEt$^-$ shows little prompt detachment signal over the $S_1(\pi\pi^*)$ band. However, a high-eKE feature with β_2 ≈-0.1 – see triangular region in Figure 5c, which is consistent with prompt detachment is evident for photon energies over the $S_2(\pi\pi^*)$ band – see example $h\nu$ = 4.28 eV spectrum in Figure 5e. There is a decrease in the intensity of the low-eKE feature for photon energies larger than ≈4.1 eV, i.e. beyond the $S_2(\pi\pi^*) \leftarrow S_0$ transition. The high-eKE feature provides the detachment parameters of ADE = 3.7±0.2 eV and VDE = 3.9±0.2 eV. Earlier electronic structure calculations at the EOM-IP-CCSD/aug-cc-pVDZ (RI-MP2/aug-cc-pVDZ geometry) level of theory determined the lowest VDE at 3.87 eV,[39] which is consistent with present experimental value.

Recent tandem ion mobility measurements on the E isomer of pCEt$^-$ did not find any evidence for $E \rightarrow Z$ photoisomerization in the gas phase.[39] Because the present study has demonstrated that a significant fraction of pCEt$^-$ molecules photoexcited over the the first two $\pi\pi^*$ states recover the ground electronic state, we conclude that the internal conversion dynamics in pCEt$^-$ do not involve a conical intersection associated with substantial torsion of the central alkene bond.

Conclusions and outlook

This investigation has demonstrated that two deprotomeric forms of methylated *para*-hydroxycinnamate molecules have diametric excited state dynamics following excitation of the first few electronic states. Whereas deprotonation on the hydroxyl group (pCEs$^-$) shows no evidence of internal conversion to recover the ground electronic state when photoexcited over the first three action-absorption bands and thus cannot undergo $E \rightarrow Z$ isomerization by passage through a conical intersection, deprotonation on the carboxylate group (pCEt$^-$) shows efficient ground state recovery dynamics when photoexcited over the first two absorption bands.

The $S_2(n\pi^*) \leftarrow S_0$ transition in pCEs$^-$ is substantially brighter than predicted from conventional excited state calculations due to Herzberg-Teller coupling, and there are apparently mode-specific internal conversion vs prompt detachment dynamics depending on whether the Franck-Condon or Herzberg-Teller modes are excited. The $2^1(\pi\pi^*)$ state in pCEs$^-$ state also exhibits complex prompt autodetachment and internal conversion excited state dynamics, with evidence for a mode-specific competition. For pCEs$^-$ at room temperature, it is hard to envisage that further single-color photoelectron studies could provide additional insight into these dynamics, rather future studies should focus on cold anions to disentangle the two possible spectral broadening effects for the $2^1(\pi\pi^*) \leftarrow S_0$ transition, and time-resolved measurements over photon energies associated with low-eKE and high-eKE electron ejection modulation to directly probe the excited state dynamics.

In the context of models for the chromophore in PYP and assuming that pCEs$^-$ behaves similarly to the actual thioester biochromophore, the lack of ground state recovery following excitation of the first three bright electronic states implies that interactions between the chromophore and the protein's binding pocket plays a key role in facilitating PYP photochemistry. Specifically, the lack of ground state recovery for pCEs$^-$ in the gas phase indicates that $E \rightarrow Z$ photoisomerization is inefficient compared with autodetachment. In accord with excited state molecular dynamics simulations[20] and recent time-resolved photoelectron spectroscopy measurements on the $S_1(\pi\pi^*)$ state of pCEs$^-$,[30] we conclude that the lack of internal conversion to the ground electronic state and associated $E \rightarrow Z$ isomerization to give a stable photoisomer is due to barriers on the $S_1(\pi\pi^*)$ state. The additional vibrational energy deposited in the $S_1(\pi\pi^*)$ state following excitation and internal conversion from the $S_2(n\pi^*)$ or $2^1(\pi\pi^*)$ states is inefficient at helping traverse these barriers before autodetachment.

Acknowledgement This research was supported by the University of East Anglia start-up allowance (to JNB), and the European Research Council's Starting Grant scheme (306536 to JRRV). The computational research presented in this paper was carried out on the High Performance Computing Cluster supported by the Research and Specialist Computing Support service at the University of East Anglia.

Conflicts of Interest

There are no conflicts of interest to declare.

Supporting Information Available

Further details of the Franck-Condon-Herzberg-Teller simulations for the $S_2(n\pi^*)$ transition in pCEs$^-$.

All photoelectron spectra that contribute to the the frequency-resolved photoelectron spectrum for pCEs$^-$ and pCEt$^-$.

References

(1) Meyer, T. E. Isolation and Characterization of Soluble Cytochromes, Ferredoxins and Other Chromophoric Proteins From the Halophilic Phototrophic Bacterium *Ectothiorhodospira halophila*. *Biochem. Biophysica Acta* **1985**, *806*, 175–183.

(2) Meyer, T. E.; Yakali, E.; Cusanovich, M. A.; Tollin, G. Properties of a Water-Soluble, Yellow Protein Isolated from a Halophilic Phototrophic Bacterium that has Photochemical Activity Analogous to Sensory Rhodopsin. *Biochem.* **1987**, *26*, 418–423.

(3) Kort, R.; Vonk, H.; Xu, X.; Hoff, W. D.; Crielaard, W.; Hellingwerf, K. J. Evidence for *trans-cis* Isomerization of the p-Coumaric Acid Chromophore as the Photochemical Basis of the Photocycle of Photoactive Yellow Protein. *FEBS Lett.* **1996**, *382*, 73–78.

(4) Schotte, F.; Cho, H. S.; Kaila, V. R. I.; Kamikubo, H.; Dashdorj, N.; Henry, E. R.; Graber, T. J.; Henning, R.; Wulff, M.; Hummer, G. et al. Watching a Signaling Protein Function in Real Time via 100-ps Time-Resolved Laue Crystallography. *Proc. Nat. Acad. Sci.* **2012**, *109*, 19256–19261.

(5) Jung, Y. O.; Lee, J. H.; Kim, J.; Schmidt, M.; Moffat, K.; Šrajer, V.; Ihee, H. Volume-Conserving *trans-cis* Isomerization Pathways in Photoactive Yellow Protein Visualized by Picosecond X-ray Crystallography. *Nat. Chem.* **2013**, *5*, 212–220.

(6) Tenboer, J.; Basu, S.; Zatsepin, N.; Pande, K.; Milathianaki, D.; Frank, M.; Hunter, M.; Boutet, S.; Williams, G. J.; Koglin, J. E. et al. Time-resolved Serial Crystallography Captures High-Resolution Intermediates of Photoactive Yellow Protein. *Science* **2014**, *346*, 1242–1246.

(7) Pande, K.; Hutchison, C. D. M.; Groenhof, G.; Aquila, A.; Robinson, J. S.; Tenboer, J.; Basu, S.; Boutet, S.; DePonte, D. P.; Liang, M. et al. Femtosecond Structural Dynamics Drives the *trans/cis* Isomerization in Photoactive Yellow Protein. *Science* **2016**, *352*, 725–729.

(8) Sprenger, W. W.; Hoff, W. D.; Armitage, J.; Hellingwerf, K. J. The Eubacterium *Ectothiorhodospira halophila* is Negatively Phototactic, with a Wavelength Dependence that Fits the Absorption Spectrum of the Photoactive Yellow Protein. *J. Bacteriol.* **1993**, *175*, 3096–3104.

(9) Pastrana, E. Optogenetics: Controlling Cell Function With Light. *Nat. Meth.* **2011**, *8*, 24–25.

(10) Deisseroth, K. Optogenetics. *Nat. Meth.* **2011**, *8*, 26–29.

(11) Baker, L. A.; Horbury, M. D.; Greenough, S. E.; Allais, F.; Walsh, P. S.; Habershon, S.; Stavros, V. G. Ultrafast Photoprotecting Sunscreens in Natural Plants. *J. Phys. Chem. Lett.* **2016**, *7*, 56–61.

(12) Tan, E. M. M.; Hilbers, M.; Buma, W. J. Excited-State Dynamics of Isolated and Microsolvated Cinnamate-Based UV-B Sunscreens. *J. Phys. Chem. Lett.* **2014**, *5*, 2464–2468.

(13) Changenet-Barret, P.; Espagne, A.; Charier, S.; Baudin, J.-B.; Jullien, L.; Plaza, P.; Hellingwerf, K. J.; Martin, M. M. Early Molecular Events in the Photoactive Yellow Protein: Role of the Chromophore Photophysics. *Photochem. Photobiol. Sci.* **2004**, *3*, 823–829.

(14) Espagne, A.; Changenet-Barret, P.; Plaza, P.; Martin, M. M. Solvent Effect on the Excited-State Dynamics of Analogues of the Photoactive Yellow Protein Chromophore. *J. Phys. Chem. A* **2006**, *110*, 3393–3404.

(15) Espagne, A.; Paik, D. H.; Changenet-Barret, P.; Martin, M. M.; Zewail, A. H. Ultrafast Photoisomerization of Photoactive Yellow Protein Chromophore Analogues in Solution: Influence of the Protonation State. *ChemPhysChem* **2006**, *7*, 1717–1726.

(16) Changenet-Barret, P.; Lacombat, F.; Plaza, P. Reaction-Coordinate Tracking in the Excited-State Deactivation of the Photoactive Yellow Protein Chromophore in Solution. *J. Photochem. Photobiol. A: Chem.* **2012**, *234*, 171–180.

(17) El-Gezawy, H.; Rettig, W.; Danel, A.; Jonusauskas, G. Probing the Photochemical Mechanism in Photoactive Yellow Protein. *J. Phys. Chem. B* **2005**, *109*, 18699–18705.

(18) Stahl, A.; Hospes, M.; Singhal, K.; van Stokkum, I.; van Grondelle, R.; Groot, M.; Hellingwerf, K. On the Involvement of Single-Bond Rotation in the Primary Photochemistry of Photoactive Yellow Protein. *Biophys. J.* **2011**, *101*, 1184–1192.

(19) Kuramochi, H.; Takeuchi, S.; Tahara, T. Ultrafast Structural Evolution of Photoactive Yellow Protein Chromophore Revealed by Ultraviolet Resonance Femtosecond Stimulated Raman Spectroscopy. *J. Phys. Chem. Lett.* **2012**, *3*, 2025–2029.

(20) Groenhof, G.; Bouxin-Cademartory, M.; Hess, B.; de Visser, S. P.; Berendsen, H. J. C.; Olivucci, M.; Mark, A. E.; Robb, M. A. Photoactivation of the Photoactive Yellow Protein: Why Photon Absorption Triggers a Trans-to-Cis Isomerization of the Chromophore in the Protein. *J. Am. Chem. Soc.* **2004**, *126*, 4228–4233.

(21) Groenhof, G.; Schäfer, L. V.; Boggio-Pasqua, M.; Grubmüller, H.; Robb, M. A. Arginine52 Controls the Photoisomerization Process in Photoactive Yellow Protein. *J. Am. Chem. Soc.* **2008**, *130*, 3250–3251.

(22) Boggio-Pasqua,; Robb, M. A.; Groenhof, G. Hydrogen Bonding Controls Excited-State Decay of the Photoactive Yellow Protein Chromophore. *J. Am. Chem. Soc.* **2009**, *131*, 13580–13581.

(23) Boggio-Pasqua, M.; Burmeister, C. F.; Robb, M. A.; Groenhof, G. Photochemical Reactions in Biological Systems: Probing the Effect of The Environment by Means of Hybrid Quantum Chemistry/Molecular Mechanics Simulations. *Phys. Chem. Chem. Phys.* **2011**, *14*, 7912–7928.

(24) Boggio-Pasqua, M.; Groenhof, G. Controlling the Photoreactivity of the Photoactive Yellow Protein Chromophore by Substituting at the *p*-Coumaric Acid Group. *J. Phys. Chem. B* **2011**, *115*, 7021–7028.

(25) Isborn, C. M.; Götz, A. W.; Clark, M. A.; Walker, R. C.; Martínez, T. J. Electronic Absorption Spectra from MM and ab Initio QM/MM Molecular Dynamics: Environmental Effects on the Absorption Spectrum of Photoactive Yellow Protein. *J. Chem. Theory Comput.* **2012**, *8*, 5092–5106.

(26) Garcia-Prieto, F. F.; Munoz-Losa, A.; Luz Sanchez, M.; Elena Martin, M.; Aguilar, M. A. Solvent Effects on De-excitation Channels in the *p*-Coumaric Acid Methyl Ester Anion, An Analogue of the Photoactive Yellow Protein (PYP) Chromophore. *Phys. Chem. Chem. Phys.* **2016**, *18*, 27476–27485.

(27) García-Prieto, F. F.; Muñoz Losa, A.; Fdez. Galván, I.; Sánchez, M. L.; Aguilar, M. A.; Martín, M. E. QM/MM Study of Substituent and Solvent Effects on the Excited State Dynamics of the Photoactive Yellow Protein Chromophore. *J. Chem. Theo. Comput.* **2017**, *13*, 737–748.

(28) Lee, I.-R.; Lee, W.; Zewail, A. H. Primary Steps of the Photoactive Yellow Protein: Isolated Chromophore Dynamics and Protein Directed Function. *Proc. Nat. Acad. Sci.* **2006**, *103*, 258.

(29) Nesbitt, D. J.; Field, R. W. Vibrational Energy Flow in Highly Excited Molecules: Role of Intramolecular Vibrational Redistribution. *J. Phys. Chem.* **1996**, *100*, 12735–12756.

(30) Bull, J. N.; Anstöter, C. S.; Verlet, J. R. R. Ultrafast Valence to Non-Valence Excited State Dynamics in a Common Anionic Chromophore. *Nat. Comm.* **2019**, *10*, 5820.

(31) Nielsen, I. B.; Boyé-Péronne, S.; El Ghazaly, M. O. A.; Kristensen, M. B.; Brøndsted Nielsen, S.; Andersen, L. H. Absorption Spectra of Photoactive Yellow Protein Chromophores in Vacuum. *Biophys. J.* **2005**, *89*, 2597–2604.

(32) Rocha-Rinza, T.; Christiansen, O.; Rajput, J.; Gopalan, A.; Rahbek, D. B.; Andersen, L. H.; Bochenkova, A. V.; Granovsky, A. A.; Bravaya, K. B.; Nemukhin, A. V. et al. Gas Phase Absorption Studies of Photoactive Yellow Protein Chromophore Derivatives. *J. Phys. Chem. A* **2009**, *113*, 9442–9449.

(33) Rocha-Rinza, T.; Christiansen, O.; Rahbek, D. B.; Klaerke, B.; Andersen, L. H.; Lincke, K.; Brøndsted Nielsen, M. Spectroscopic Implications of the Electron Donor-Acceptor Effect in the Photoactive Yellow Protein Chromophore. *Chem. Eur. J.* **2010**, *16*, 11977–11984.

(34) Almasian, M.; Grzetic, J.; van Maurik, J.; Steill, J. D.; Berden, G.; Ingemann, S.; Buma, W. J.; Oomens, J. Non-Equilibrium Isomer Distribution of the Gas-Phase Photoactive Yellow Protein Chromophore. *J. Phys. Chem. Lett.* **2012**, *3*, 2259–2263.

(35) Mooney, C. R. S.; Parkes, M. A.; Iskra, A.; Fielding, H. H. Controlling Radical Formation in the Photoactive Yellow Protein Chromophore. *Angew. Chem. Int. Ed.* **2015**, *54*, 5646–5649.

(36) Parkes, M. A.; Phillips, C.; Porter, M. J.; Fielding, H. F. Controlling Electron Emission From the Photoactive Yellow Protein Chromophore by Substitution at the Coumaric Acid Group. *Phys. Chem. Chem. Phys.* **2016**, *18*, 10329–10336.

(37) Henley, A.; Diveky, M. E.; Patel, A. M.; Parkes, M. A.; Anderson, J. C.; Fielding, H. H. Electronic Structure and Dynamics of Torsion-Locked Photoactive Yellow Protein Chromophores. *Phys. Chem. Chem. Phys.* **2017**, *19*, 31572–31580.

(38) Henley, A.; Diveky, M. E.; Patel, A. M.; Parkes, M. A.; Anderson, J. C.; Fielding, H. H. The Role of Photoisomerisation on the Photodetachment of the Photoactive Yellow Protein Chromophore. *J. Phys. Chem. A* **2018**, *122*, 8222–8228.

(39) Bull, J. N.; da Silva, G.; Scholz, M. S.; Carrascosa, E.; Bieske, E. J. Photoinduced Intramolecular Proton Transfer in Deprotonated *para*-Coumaric Acid. *J. Phys. Chem. A* **2019**, *123*, 4419–4430.

(40) Matthews, E.; Dessent, C. E. H. Experiment and Theory Confirm That UV Laser Photodissociation Spectroscopy Can Distinguish Protomers Formed via Electrospray. *Phys. Chem. Chem. Phys.* **2017**, *19*, 17434–17440.

(41) Xia, H.; Attygalle, A. B. Effect of Electrospray Ionization Source Conditions on the Tautomer Distribution of Deprotonated *p*-Hydroxybenzoic Acid in the Gas Phase. *Anal. Chem.* **2016**, *88*, 6035–6043.

(42) Bull, J. N.; Coughlan, N. J. A.; Bieske, E. J. Protomer-Specific Photochemistry Investigated Using Ion Mobility Mass Spectrometry. *J. Phys. Chem. A* **2017**, *121*, 6021–6027.

(43) Roberts, G. M.; Lecointre, J.; Horke, D. A.; Verlet, J. R. R. Spectroscopy and Dynamics of the 7,7,8,8-tetracyanoquinodimethane Radical Anion. *Phys. Chem. Chem. Phys.* **2010**, *12*, 6226–6232.

(44) Horke, D. A.; Roberts, G. M.; Lecointre, J.; Verlet, J. R. R. Velocity-Map Imaging at Low Extraction Fields. *Rev. Sci. Instrum.* **2012**, *83*, 063101.

(45) West, C. W.; Bull, J. N.; Antonkov, E.; Verlet, J. R. R. Anion Resonances of *para*-Benzoquinone Probed by Frequency-Resolved Photoelectron Imaging. *J. Phys. Chem. A* **2014**, *118*, 11346–11354.

(46) Bull, J. N.; West, C. W.; Verlet, J. R. R. On the Formation of Anions: Frequency-, Angle-, and Time-Resolved Photoelectron Imaging of the Menadione Radical Anion. *Chem. Sci.* **2015**, *6*, 1578–1589.

(47) Roberts, G. M.; Nixon, J. L.; Lecointre, J.; Wrede, E.; Verlet, J. R. R. Toward Real-Time Charged-Particle Image Reconstruction Using Polar Onion-Peeling. *Rev. Sci. Instrum.* **2009**, *80*, 053104.

(48) Zare, R. N. Photoejection Dynamics. *Mol. Photochem.* **1972**, *4*, 1–37.

(49) Bull, J. N.; West, C. W.; Verlet, J. R. R. Internal Conversion Outcompetes Autodetachment From Resonances in the Deprotonated Tetracene Anion Continuum. *Phys. Chem. Chem. Phys.* **2015**, *17*, 32464–32471.

(50) Small, G. J. Herzberg-Teller Vibronic Coupling and the Duschinsky Effect. *J. Chem. Phys.* **1971**, *54*, 3300–3306.

(51) Frisch, M. J.; Trucks, G. W.; Schlegel, H. B.; Scuseria, G. E.; Robb, M. A.; Cheeseman, J. R.; Scalmani, G.; Barone, V.; Mennucci, B.; Petersson, G. A. et al. Gaussian 16 Revision B.01. Gaussian Inc. Wallingford CT 2016.

(52) Santoro, F.; Lami, A.; Improta, R.; Bloino, J.; Barone, V. Effective Method for the Computation of Optical Spectra of Large Molecules at Finite Temperature Including the Duschinsky and Herzberg-Teller Effect: The Qx Band of Porphyrin as a Case Study. *J. Chem. Phys.* **2008**, *128*, 224311.

(53) Chai, J.-D.; Head-Gordon, M. Long-Range Corrected Hybrid Density Functionals With Damped Atom-Atom Dispersion Corrections. *Phys. Chem. Chem. Phys.* **2008**, *10*, 6615–6620.

(54) Dunning, Jr., J. T. H. Gaussian Basis Sets for Use in Correlated Molecular Calculations. I. The Atoms Boron Through Neon and Hydrogen. *J. Chem. Phys.* **1989**, *90*, 1007.

(55) Dutta, A. K.; Saitow, M.; Demoulin, B.; Neese, F.; Izsák, R. A Domain-Based Local Pair Natural Orbital Implementation of the Equation of Motion Coupled Cluster Method for Electron Attached States. *J. Chem. Phys.* **2019**, *150*, 164123.

(56) Neese, F. The ORCA Program System. *WIRES Comp. Mol. Sci.* **2012**, *2*, 73–78.

(57) Herzberg, G.; Teller, E. Schwingungsstruktur der Elektronenübergänge bei mehratomigen Molekülen. *Zeitsch. für Physik. Chem.* **1933**, *21B*, 410–446.

(58) Orlandi, G.; Siebrand, W. Theory of Vibronic Intensity Borrowing. Comparison of Herzberg-Teller and Born-Oppenheimer Coupling. *J. Chem. Phys.* **1973**, *58*, 4513–4523.

(59) Lin, S. H.; Eyring, H. Study of the Franck-Condon and Herzberg-Teller Approximations. *Proc. Nat. Acad. Sci.* **1974**, *71*, 3802–3804.

(60) Taylor, H. S.; Nazaroff, G. V.; Golebiewski, A. Qualitative Aspects of Resonances in Electron-Atom and Electron-Molecule Scattering, Excitation, and Reactions. *J. Chem. Phys.* **1966**, *45*, 2872–2888.

(61) Schiedt, J.; Weinkauf, R. Resonant Photodetachment via Shape and Feshbach Resonances: *p*-benzoquinone Anions as a Model System. *J. Chem. Phys.* **1999**, *110*, 304–314.

(62) Horke, D. A.; Li, Q.; Blancafort, L.; Verlet, J. R. R. Ultrafast Above-Threshold Dynamics of the Radical Anion of a Prototypical Quinone Electron-Acceptor. *Nat. Chem.* **2013**, *5*, 711–717.

(63) Bull, J. N.; Scholz, M. S.; Carrascosa, E.; da Silva, G.; Bieske, E. J. Double Molecular Photoswitch Driven by Light and Collisions. *Phys. Rev. Lett.* **2018**, *120*, 223002.

(64) Anstöter, C. S.; Bull, J. N.; Verlet, J. R. R. Ultrafast Dynamics of Temporary Anions Probed Through the Prism of Photodetachment. *Int. Rev. Phys. Chem.* **2016**, *35*, 509–538.

(65) West, C. W.; Bull, J. N.; Hudson, A. S.; Cobb, S. L.; Verlet, J. R. R. Excited State Dynamics of the Isolated Green Fluorescent Protein Chromophore Anion Following UV Excitation. *J. Phys. Chem. B* **2015**, *119*, 3982–3987.

(66) Anstöter, C. S.; Dean, C. R.; Verlet, J. R. R. Chromophores of Chromophores: A Bottom-up Hückel Picture of the Excited States of Photoactive Proteins. *Phys. Chem. Chem. Phys.* **2017**, *19*, 29772–29779.

(67) Bochenkova, A. V.; Mooney, C. R. S.; Parkes, M. A.; Woodhouse, J. L.; Zhang, L.; Lewin, R.; Ward, J. M.; Hailes, H. C.; Andersen, L. H.; Fielding, H. H. Mechanism of Resonant Electron Emission From the Deprotonated GFP Chromophore and Its Biomimetics. *Chem. Sci.* **2017**, *8*, 3154–3163.

(68) Glover, W. J.; Paz, A. S. P.; Thongyod, W.; Punwong, C. Analytical Gradients and derivative couplings for dynamically weighted complete active space Self-Consistent Field. *J. Chem. Phys.* **2019**, *151*, 201101.

(69) Bull, J. N.; West, C. W.; Verlet, J. R. R. Ultrafast Dynamics of Formation and Autodetachment of a Dipole-Bound State in an Open-Shell π-Stacked Dimer Anion. *Chem. Sci.* **2016**, *7*, 5352–5361.

(70) Bull, J. N.; Verlet, J. R. R. Observation and Ultrafast Dynamics of a Nonvalence Correlation-Bound State of an Anion. *Sci. Adv.* **2017**, *3*, e1603106.

(71) Simons, J. Propensity Rules for Vibration-Induced Electron Detachment of Anions. *J. Am. Chem. Soc.* **1981**, *103*, 3971–3976.

(72) Jordan, K. D.; Wang, F. Theory of Dipole-Bound Anions. *Ann. Rev. Phys. Chem.* **2003**, *54*, 367–396.

Graphical TOC Entry